Isotopic enrichment of silicon by high fluence ^{28}Si$^-$ ion implantation

D. Holmes [1,*] B. C. Johnson,[1] C. Chua [2,3] B. Voisin,[2,3] S. Kocsis,[2,3] S. Rubanov [4] S. G. Robson [1] J. C. McCallum,[1]
D. R. McCamey,[5] S. Rogge,[6] and D. N. Jamieson [1]

[1]*Centre for Quantum Computing and Communication Technology, School of Physics, The University of Melbourne,
Melbourne VIC 3010, Australia*
[2]*Silicon Quantum Computing, Sydney NSW 2052, Australia*
[3]*School of Physics, University of New South Wales Sydney, Sydney NSW 2052, Australia*
[4]*Advanced Microscopy Facility, Bio21 Institute, The University of Melbourne, Melbourne VIC 3010, Australia*
[5]*ARC Centre of Excellence in Exciton Science, School of Physics, University of New South Wales, Sydney NSW 2052, Australia*
[6]*Centre for Quantum Computation and Communication Technology, School of Physics, University of New South Wales Sydney,
Sydney NSW 2052, Australia*

Spins in the "semiconductor vacuum" of silicon-28 (^{28}Si) are suitable qubit candidates due to their long coherence times. An isotopically purified substrate or epilayer of ^{28}Si is required to limit the decoherence pathway caused by magnetic perturbations from surrounding ^{29}Si nuclear spins ($I = 1/2$), present in natural Si (^{nat}Si) at an abundance of 4.67%. We isotopically enrich surface layers of ^{nat}Si by sputtering using high fluence ^{28}Si$^-$ implantation. Phosphorus (P) donors implanted into one such ^{28}Si layer with $\sim$3000 ppm ^{29}Si, produced by implanting 30 keV ^{28}Si$^-$ ions at a fluence of 4×10^{18} cm^{-2}, were measured with pulsed electron spin resonance, confirming successful donor activation upon annealing. The monoexponential decay of the Hahn echo signal indicates a depletion of ^{29}Si. A coherence time of $T_2 = 285 \pm 14$ μs is extracted, which is longer than that obtained in ^{nat}Si for similar doping concentrations and can be increased by reducing the P concentration in the future. Guided by simulations, the isotopic enrichment was improved by employing one-for-one ion sputtering using 45 keV ^{28}Si$^-$ implanted with a fluence of 2.63×10^{18} cm^{-2} into ^{nat}Si. This resulted in an isotopically enriched surface layer $\sim$100 nm thick, suitable for providing a sufficient volume of ^{28}Si for donor qubits implanted into the near-surface region. We observe a depletion of ^{29}Si to 250 ppm as measured by secondary ion mass spectrometry. The impurity content and the crystallization kinetics via solid phase epitaxy are discussed. The ^{28}Si layer is confirmed to be a single crystal using transmission electron microscopy. This method of Si isotopic enrichment shows promise for incorporation into the fabrication process flow of Si spin-qubit devices.

I. SPINS IN ^{28}Si

Donor and quantum dot spin qubits in silicon (Si) are attractive candidates for high-fidelity scalable quantum computing architectures [1–3]. Si provides a desirable matrix for hosting spin qubits due to its important role in the microelectronics industry, weak spin-orbit coupling, and the existence of isotopes with zero nuclear spin. Natural Si consists of three isotopes: ^{28}Si (92.23%), ^{29}Si (4.67%), and ^{30}Si (3.1%) [4]. A significant source of qubit decoherence in ^{nat}Si is due to coupling with the surrounding ^{29}Si nuclei, which possess a nuclear spin of $I = 1/2$. Dipolar fluctuations of ^{29}Si spins cause perturbations in the local magnetic field, resulting in a time-varying qubit resonance frequency [5,6]. This spectral diffusion limits the spin coherence time to around 200 μs for electrons [7] and 60 ms for ionized donor nuclei [8], as measured for a single phosphorus (P) donor at low temperature using the Hahn-echo pulse sequence.

Fortunately, ^{28}Si has no nuclear spin and can therefore provide an ideal low-noise environment for spin qubits. Minimizing the number of ^{29}Si nuclei within the Bohr radius of the donor electron ($\sim$2 nm for ^{31}P in Si [9]) reduces the coupling of the donor electron to the dynamics of the ^{29}Si spin-bath through the contact hyperfine interaction [6]. Long coherence times for donor spin qubits in a ^{28}Si epilayer with 800 ppm residual ^{29}Si [10] have been demonstrated, with Hahn-echo decay times of around 1 ms for electrons and 1.75 s for single ionized ^{31}P donor nuclei at 100 mK, which can be further extended with dynamical decoupling [11]. Isotope engineering of semiconductor materials also has applications for increased thermal conductivity [12–14], capable of improved heat dissipation in Si integrated circuits [15].

Isotopically enriched ^{28}Si can be produced by various methods, many of which involve the centrifugation of silicon tetrafluoride gas to produce high-purity ^{28}Si F$_4$ [16–22]. In the Avogadro Project [20], ^{28}Si F$_4$ is converted into isotopically pure silane gas, ^{28}Si H$_4$, which is used to grow polycrystalline ^{28}Si by chemical vapor deposition (CVD). Float-zone growth is then used to produce ^{28}Si single-crystal rods. An isotopic purity of < 10 ppm ^{29}Si and the highest chemical purity to date ($<4 \times 10^{15}$ cm^{-3} for C and $<4 \times 10^{14}$ cm^{-3}

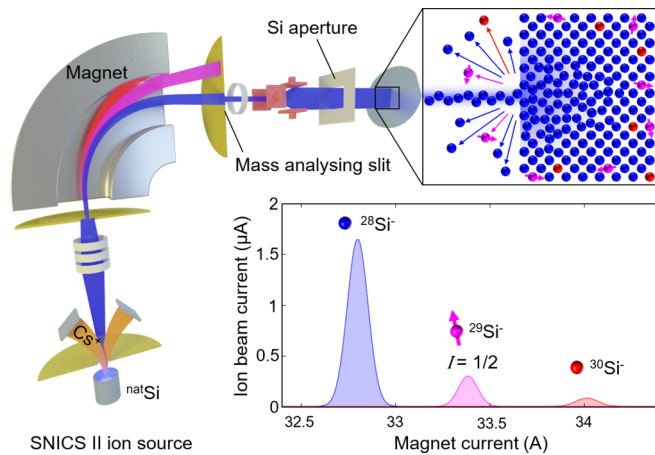*Author to whom all correspondence should be addressed: dholmes1@student.unimelb.edu.au

FIG. 1. A ^{28}Si$^-$ ion beam, filtered by a mass-selecting magnet from a solid ^{nat}Si source, is used to isotopically enrich a ^{nat}Si substrate surface layer by sputtering. The mass spectrum of the ion implanter shows the isotopic resolution of Si.

for O) was achieved [22]. Epilayers of ^{28}Si can be grown on 300 mm ^{nat}Si substrates by CVD [23,24] (a method employed by the Isonics Corporation [10]) or molecular beam epitaxy [25–27] (suitable for encapsulation of scanning tunneling microscopy-placed donors in ^{28}Si [28,29]). These methods rely on isotopically enriched sources of silane gas or solid-state ^{28}Si. Mass spectrometry, on the other hand, can be used to separate ^{28}Si ions from a natural silane gas source. This has been used in conjunction with hyperthermal energy ion beam deposition to achieve a residual ^{29}Si fraction of <1 ppm in a layer of ^{28}Si [30,31]. However, the concentration of C and O was >1 × 10^{19} cm^{-3} [30]. The epitaxial growth of ^{28}Si thin films by ion beam deposition with a solid ^{nat}Si source has also been achieved by depositing low energy (~40 eV) ^{28}Si$^-$ ions [32].

In this work, we achieve isotopic enrichment through sputtering by implanting a high fluence of ^{28}Si$^-$ ions, mass-separated from an accelerated ion beam produced from a solid-state ^{nat}Si source, into a ^{nat}Si substrate, shown schematically in Fig. 1. Since any isotope in the substrate can be sputtered from the surface, but only ^{28}Si ions are implanted, the levels of ^{29}Si and ^{30}Si are depleted with increasing fluence. This results in an enriched surface layer of ^{28}Si with sufficient volume for donor qubits, typically implanted to a depth of around 20 nm below the Si surface for effective control and readout by surface nanocircuitry [33]. Production of this material has the advantage of using standard ion beam laboratory equipment, enabling the integration of *in situ* enrichment with existing ion-implanted donor qubit fabrication [34]. Additionally, the creation of an amorphous ^{28}Si layer increases the placement precision of implanted donors by suppressing ion channeling [35], and it can increase the donor electrical activation yield [36]. Solid phase epitaxy (SPE) of an amorphous Si (*a*-Si) surface layer formed by Si implantation can produce near-perfect single-crystal Si (*c*-Si) [37] with a smooth surface [38], in which no long-range atomic displacement occurs [39]. A one-for-one replacement implant regime resulting in a planar Si surface (suitable for postfabrication of nanocircuitry)

could allow for economical local enrichment of regions using a focused ^{28}Si ion beam into which donors are implanted.

The concentration of impurities introduced to the enriched layer during high fluence ^{28}Si implantation must be minimized, with particular care taken to avoid coimplantation of the molecular isobars CO and N$_2$. The presence of C, N, and O in the *a*-Si layer at levels of around 0.5 at. % causes retardation of the SPE regrowth rate [40] and can lead to polycrystalline nucleation during annealing at sufficient concentrations [41]. The use of a negative ^{28}Si ion beam ensures a negligible component of the isobars CO and N$_2$, since these negatively charged molecular ions are electronically unstable.

In the present work, 30–45 keV ^{28}Si$^-$ ions were implanted at a high fluence into ^{nat}Si. The crystallization kinetics were determined using time-resolved reflectivity (TRR), and the coherence time of P donors implanted into the enriched ^{28}Si layer was measured using pulsed electron spin resonance (ESR). The extent of ^{29}Si depletion and impurity levels introduced was measured using secondary ion mass spectrometry (SIMS). The concentration of impurities was sufficiently low to allow for crystallization to take place via SPE, resulting in a single-crystal layer of ^{28}Si, as shown by transmission electron microscopy (TEM).

II. EXPERIMENT

To isotopically enrich ^{nat}Si substrates, a 150 keV ion implanter, equipped with a SNICS II ion source and a 90° double focusing magnet, was used. Figure 1 schematically shows the mass spectrum of this implanter with a ^{nat}Si source, demonstrating the mass resolution of the Si isotopes. Near the start of an implant run, the ion beam currents for ^{29}Si$^-$ and ^{30}Si$^-$ are higher than their natural abundance as they contain a significant fraction of ^{28}Si H$^-$ and ^{29}Si H$^-$, respectively. ^{28}Si$^-$ implants were performed at room temperature with a 7° substrate tilt off the incident beam axis to suppress ion channeling. A Si aperture, prepared from a wafer of ^{nat}Si, was used to collimate the beam and prevent contamination from forward recoils of foreign atoms. Substrates were given a degreasing clean and a HF etch to remove surface hydrocarbons and native oxide before entering the implant chamber to further reduce contamination. A vacuum of less than 1 × 10^{-7} Torr was maintained in the target chamber with a cryopump to reduce impurity incorporation from residual gas by ion bombardment.

Samples A and B were prepared according to Table I by implanting highly intrinsic (4–10 kΩ cm) float-zone uniform

TABLE I. Implant parameters for samples A and B.

	Sample A	Sample B
^{28}Si$^-$ implant energy (keV)	30	45
^{28}Si$^-$ implant fluence (cm^{-2})	4 × 10^{18}	2.63 × 10^{18}
^{31}P$^-$ implants (keV, cm^{-2})	30, 6.5 × 10^{11} 10, 1.5 × 10^{11}	
Anneal(s) (°C, s, ambient)	609, 394, air	620, 600, Ar 1000, 5, Ar

high-purity ^{nat}Si (UHPS Topsil) substrates with a high fluence of ^{28}Si$^-$ ions followed by, in the case of Sample A, ^{31}P$^-$ implantation. Both samples were given a piranha (4:1 98% H$_2$SO$_4$: 30% H$_2$O$_2$, 90 °C) and RCA-2 (5:1:1 H$_2$O : 30% H$_2$O$_2$: 36% HCl, 70 °C) clean before thermal annealing to facilitate SPE growth and donor activation. The properties of sample A were investigated using TRR, SIMS, and pulsed ESR, while sample B was characterized with SIMS and TEM, as discussed in the following.

III. SAMPLE A: ESR AT 3000 ppm ^{29}Si

To investigate the crystallization kinetics of the enriched a-Si layer in sample A, TRR [42] was used with a laser wavelength of $\lambda = 632.8$ nm during an anneal in air at 609 °C. The rate of crystallization was compared to an a-Si standard: n-type ^{nat}Si amorphized with a much lower fluence of ^{28}Si$^-$ ions with the following implantation scheme: (0.5 MeV, 3×10^{15} cm^{-2}), then (1 MeV, 1×10^{15} cm^{-2}), and finally (2 MeV, 1×10^{15} cm^{-2}). The SPE growth rate of this a-Si standard during the initial stages of the anneal was used to calibrate the temperature of the TRR heating stage. Refractive indices of $n_c = 4.086$ for c-Si [43] and $n_a = 4.831$ for a-Si [42] were used for the SPE rate calculation.

TRR showed the complete crystallization of the a-Si layer in sample A via thermally activated SPE with an intrinsic rate described by the Arrhenius relationship:

$$v_i = v_0 \exp(E_A / k_B T) \qquad (1)$$

with $E_A = 2.70$ eV and $v_0 = 4.64 \times 10^{16}$ Å/s [44]. The SPE rate of the a-Si standard was calculated from the TRR curve to be 17.3 Å/s, whereas that of sample A was 8.9 Å/s. The increased level of impurities [40] and open-volume defects [45] introduced by high fluence implantation slows the progression of the a/c interface.

After annealing, the isotopic enrichment level of sample A was measured with SIMS (IONTOF GmbH, TOF.SIMS 5). The Si isotopes were measured in negative polarity with a 1 keV Cs$^+$ beam used for sputtering and a 30 keV Bi$^+$ beam used for analysis. Experimental results displayed on the left axis of Fig. 2(a) show ^{29}Si and ^{30}Si are depleted in the surface $\sim$50 nm of sample A to around 3000 and 2000 ppm, respectively. ^{31}P$^-$ was implanted into the ^{28}Si layer with a depth profile, simulated using SRIM [46], shown on the right axis of Fig. 2(a). This implant results in a P concentration of $<1.4 \times 10^{17}$ cm^{-3} throughout the enriched ^{28}Si layer, chosen to lie above the minimum detection limit of the pulsed ESR setup. The maximum P concentration was confirmed to lie below the detection limit of the SIMS equipment used in this work ($\sim$2 $\times 10^{17}$ cm^{-3}).

Pulsed ESR was performed on P donors implanted in the ^{28}Si layer of sample A after SPE. The sample was mounted onto the surface of a superconducting cavity made by dry etching a 100-nm-thick NbTiN film [47,48]. The sample, along with the cavity, was mounted on the mixing chamber of a dilution refrigerator, with a base temperature of $\sim$16 mK. Pulses were sent to the cavity using a vector source at the resonant frequency of the cavity ($f = 6.028$ GHz), and the detected echo signal was then preamplified and measured using a digitizer [47]. The ESR spectrum was obtained by varying
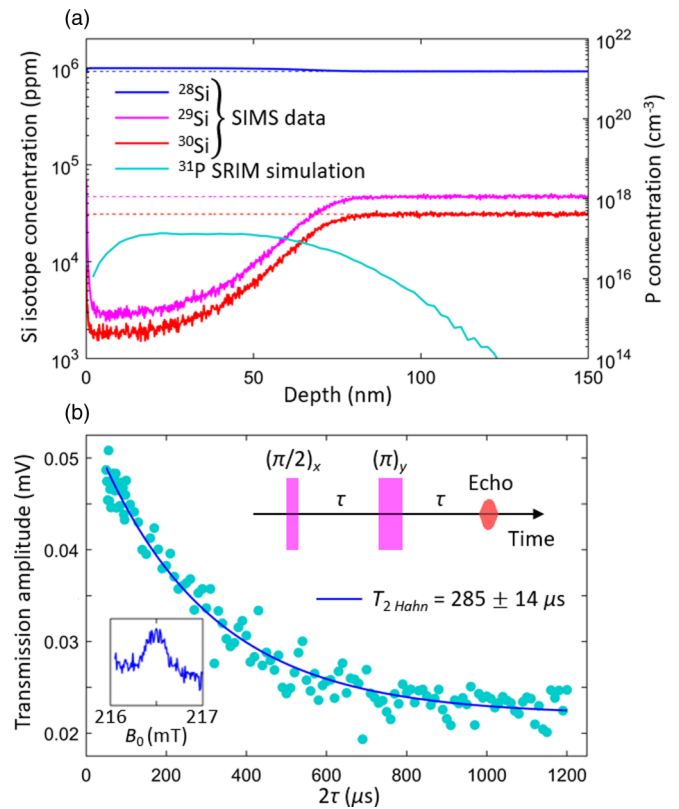

FIG. 2. Experimental data for sample A after annealing. (a) Left axis: SIMS depth profiles showing the concentration of Si isotopes as a function of depth below the surface. Natural abundance is indicated with dashed lines. Right axis: SRIM simulation of the implanted P depth profile. (b) Pulsed ESR measurement of the implanted P donors. The Hahn echo is fitted with a monoexponential decay, indicative of a ^{28}Si substrate, giving $T_2 = 285 \pm 14$ μs. The pulse sequence is shown in the top right and the upper hyperfine-split P ESR peak, collected with $\tau = 5$ μs, is shown in the bottom left.

the external magnetic field, B_0, which confirmed the presence of P by the observation of the two hyperfine-split peaks due to the nuclear spin of ^{31}P [49]. The T_2 was measured by setting the magnetic field to the value corresponding to the center of the upper hyperfine-split P peak and using a standard Hahn echo pulse sequence [47], where the pulse length (400 ns) and power were chosen such that the spins undergo a $\pi/2$ rotation for the first pulse. Due to the long T_1 of P donor electrons, the sample was illuminated with light of wavelength 1025 nm for 100 ms between each repetition of the pulse sequence in order to rapidly thermalize the donor spins [50].

The upper hyperfine-split P ESR peak, shown as an inset in Fig. 2(b), has a linewidth of $\sim$0.25 mT which is similar to that found in ^{nat}Si [51]. This broad linewidth is likely due to the B_0 field inhomogeneity or the bandwidth of the cavity used in this setup, which prevents us from observing the effect of ^{29}Si depletion. However, by varying the time between pulses, τ, in the Hahn echo pulse sequence, we obtain a monoexponential decay curve that can be fitted with a transverse relaxation time $T_2 = 285 \pm 14$ μs, as shown in Fig. 2(b). The monoexponential shape of the curve indicates that the dominant decoherence mechanism in this sample is due to instantaneous diffusion

between the donor electrons, instead of spectral diffusion from [29]Si, which manifests itself in the decay as a cubic term in the exponential fit [50–53]. In addition, the value of T_2 is comparable to previous reports for P donors in [28]Si with concentrations between 1×10^{16} and 1×10^{17} cm^{-3} [51,54] and longer than the coherence time obtained in [nat]Si for a similar doping concentration of 1.3×10^{17} cm^{-3} ($\sim$100 μs [52]). While the monoexponential decay curve and the value of T_2 do not provide us with an exact estimate for the residual [29]Si concentration, it provides evidence that our sample has a lower [29]Si concentration compared to [nat]Si. In future, the concentration of P and residual [29]Si can be further reduced to improve coherence time.

IV. TRIDYN SIMULATIONS

To improve the enrichment process, the implantation of [28]Si at various energies and fluences into [nat]Si was simulated using TRIDYN, a binary collision Monte Carlo simulation package [55]. An initial interval spacing of 5 Å was chosen to be longer than the mean free path but small enough to avoid artifacts from a coarse grid [56]. A high statistical quality was achieved using a precision of 0.02 to keep the maximum relative change of layer areal density per projectile to <0.2%.

The sputter yield as a function of implantation energy was determined for an implantation of 1×10^{17} cm^{-2} [28]Si ions at normal incidence, as shown in Fig. 3. The sputter yield dependence on implantation energy shown here is in agreement with previous experimental Si sputter yields [57,58] and theoretical fits [59]. An energy of < 3 keV results in the deposition of [28]Si onto the Si surface. If the sputter yield is greater than 1, the surface layer will be eroded faster than it can be isotopically enriched, resulting in a thin [28]Si surface layer with reduced enrichment. [28]Si ions with energies > 45 keV are implanted deeper below the surface and sputtering is suppressed, resulting in accumulation. This is desirable for producing a thick layer of [28]Si with a high level of enrichment; however, the surface will not be planar. A sputter yield of 1 is achieved at energies around 3 and 45 keV, both of which result in a planar surface, desirable for surface nanocircuitry
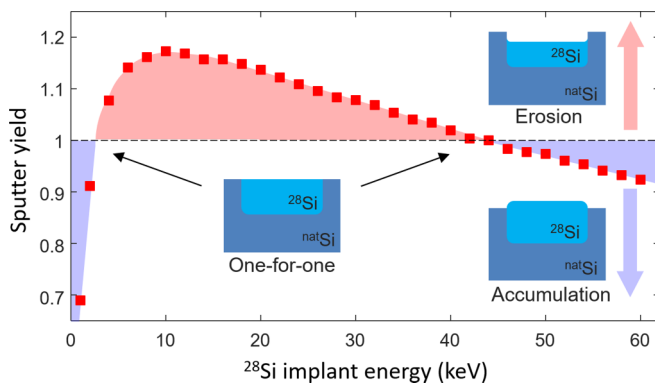

FIG. 4. TRIDYN simulation of the implantation of 45 keV [28]Si ions into [nat]Si. The dashed lines indicate natural abundance. (a) The concentration of silicon isotopes as a function of depth after an implantation fluence of 5×10^{18} cm^{-2}. (b) The concentration of [29]Si and [30]Si at a depth of 20 nm below the surface as a function of implanted fluence. Lines of best fit are displayed for both isotopes. The star symbols represent the isotope concentrations achieved in this work with sample B, extracted from Fig. 5 (see the text).

FIG. 3. TRIDYN simulation of the implantation of [28]Si ions into [nat]Si showing the sputter yield as a function of implant energy at a fluence of 1×10^{17} cm^{-2}. Schematics of the postimplantation surface are shown in the erosion, one-for-one replacement, and accumulation regimes.

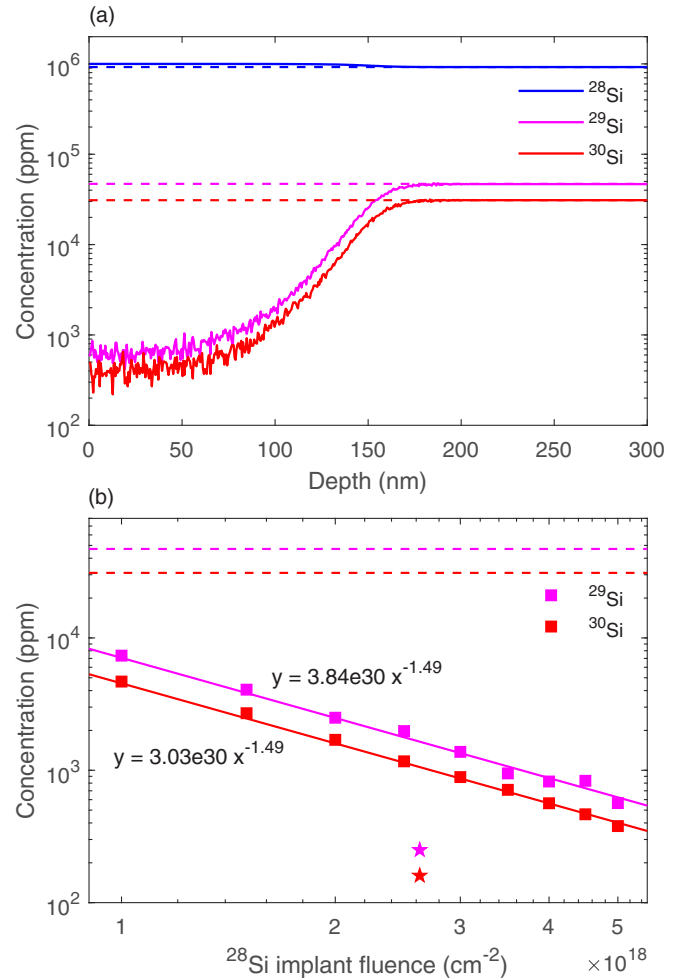fabrication. 45 keV was selected in order to produce a [28]Si surface layer thicker than the qubit target depth of $\sim$20 nm in the one-for-one replacement regime and to optimize the transmission of the ion beam through the implanter. The sputter yield is independent of angle of incidence for angles below $10°$ for self-implanted Si [58], and so the TRIDYN simulations performed here at normal incidence are applicable for our experimental implants performed with a $7°$ substrate tilt.

The simulated depth profiles of Si isotopes in [nat]Si after the implantation of 45 keV [28]Si at a fluence of 5×10^{18} cm^{-2} are shown in Fig. 4(a). This shows that an isotopically enriched surface layer $\sim$100 nm thick is created. The resultant concentrations of [29]Si and [30]Si at a depth of 20 nm below the surface as a function of fluence of 45 keV [28]Si are shown in Fig. 4(b). This shows the trend of an increased isotopic purity resulting from an increased implant fluence. The isotope concentrations

at a depth of 20 nm realized in this work with sample B as discussed below are indicated with star symbols in Fig. 4(b).

V. SAMPLE B: DEPLETING ^{29}Si TO 250 ppm

The composition with depth of sample B after annealing was obtained with the same SIMS setup and parameters as used for sample A. The measured concentrations of Si isotopes and ^{12}C and ^{12}O impurities are displayed as a function of depth below the surface in Fig. 5.

Figure 5(a) shows ^{29}Si and ^{30}Si are depleted in the surface $\sim$100 nm of sample B to around 250 and 160 ppm, respectively. The level of isotopic enrichment achieved here with 45 keV ^{28}Si$^-$ is better than that achieved with 30 keV, despite the lower implant fluence, as it is no longer limited by the self-sputtering of Si that occurs when the sputter yield is greater than 1. The shape of the isotope concentration profiles agrees well with the TRIDYN simulation shown in Fig. 4(a). A higher level of enrichment was achieved experimentally than predicted by TRIDYN, as shown by the star symbols in

FIG. 5. Experimental SIMS depth profiles for sample B after annealing. (a) The concentration of the isotopes of ^{nat}Si as a function of depth below the surface. Natural abundance is indicated with dashed lines. (b) The concentration of the impurities ^{12}C and ^{12}O as a function of depth, calibrated with typical maximum background impurity levels expected in UHPS Topsil. Dashed lines indicate the SIMS depth profiles for the nonimplanted substrate.

Fig. 4(b). This suggests that the experimental sputter yield is slightly less than 1, leading to the accumulation of a thicker isotopically enriched layer, as evidenced by the depth where the isotope concentrations reach natural abundance: $\sim$180 nm for the TRIDYN simulation [Fig. 4(a)] and $\sim$220 nm for the experimental measurement [Fig. 5(a)]. This accumulation was shown to result in lower ^{29}Si and ^{30}Si concentrations, demonstrated by TRIDYN simulations implanting > 45 keV Si (not shown). The discrepancy in sputter yield, sensitive to the target surface binding energy, could be due to the impurity content of the substrate [59]. A smaller contribution could come from the uncertainty in the experimental implantation fluence ($\sim$10%). The residual ^{29}Si concentration achieved here is around three times lower than that found in a commercially produced ^{28}Si wafer (Isonics), which, with 800 ppm ^{29}Si [10], has previously demonstrated increased coherence times of implanted donors [11].

Figure 5(b) shows the concentrations of ^{12}C and ^{12}O in an implanted region (solid lines) and in a nonimplanted region of sample B (dashed lines). The concentrations are increased above the background levels to around 1×10^{17} cm^{-3} for C and 3×10^{17} cm^{-3} for O by the process of high fluence implantation of ^{28}Si$^-$ ions and subsequent annealing. The concentrations of these impurities were calibrated by assuming that the background levels at a depth of $\sim$300 nm, which match for the implanted and nonimplanted regions, were 5×10^{15} cm^{-3}, the maximum expected background contamination for UHPS Topsil quoted by the supplier. SIMS shows that the nonimplanted substrate has an increase in impurity levels, significantly above the background level in the surface $\sim$30 nm for C and the surface $\sim$20 nm for O. This accounts for some of the near-surface impurity content in the implanted region. The O contamination is unlikely to arise from a native oxide, typically $\sim$2 nm thick, since TRIDYN simulations (not shown) confirm that the majority would be sputtered away during high fluence implantation. The Si aperture reduced forward recoils of impurities, with no trace of heavy metals detected with high-resolution Rutherford backscattering spectrometry [60] (not shown). The majority of the C and O contamination is proposed to be incorporated into the implanted layer from the imperfect vacuum, as seen in other experiments with high fluence implantation in a cryopumped target chamber [61]. Fortunately, these levels of contamination are comparable to those present in Czochralski-grown Si [(4×10^{17})–(2×10^{18}) cm^{-3} for O and (2×10^{16})–(4×10^{17}) cm^{-3} for C [62]] and indeed are shown to be low enough to allow for the successful crystallization of the enriched layer by SPE. A peak in the concentration of C and O impurities occurs at around 190 nm below the surface of Si. This could be associated with the presence of open volume defects arising from vacancy clustering, which have been observed to act as gettering sites for impurities during annealing [63,64]. Additionally, Fig. 5(b) shows preferential diffusion of C and O toward the surface, known to be a vacancy-rich region after ion implantation [65].

TEM was used to determine the crystal quality of the ^{28}Si layer in sample B after annealing. Before lamella preparation, the sample was coated with an $\sim$20-nm-thick protective carbon layer. To prepare the sample, a focused ion beam (FEI, Nova Nanolab 200) was used to grow a 300-nm-thick layer of
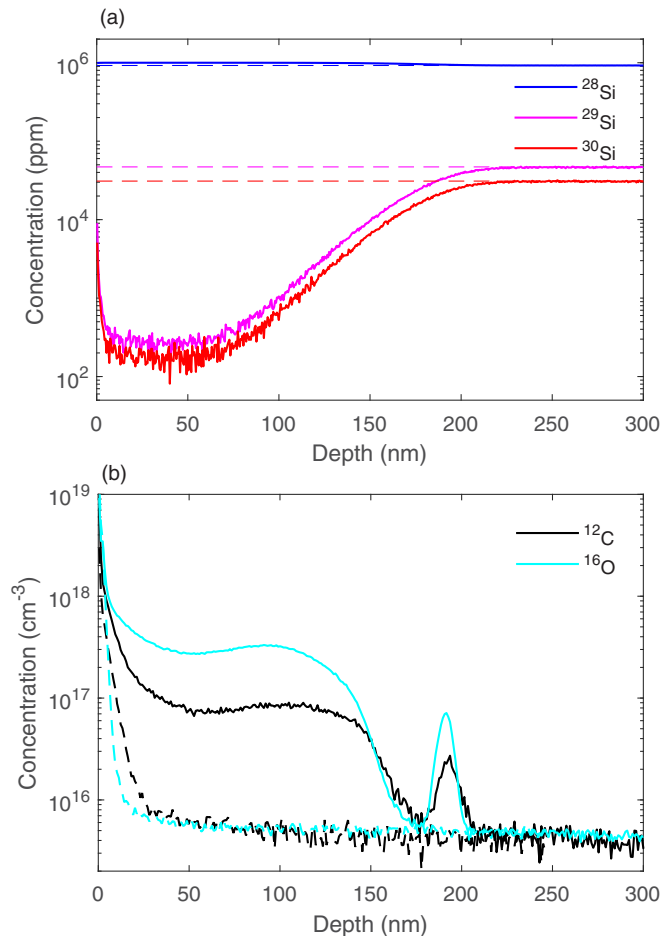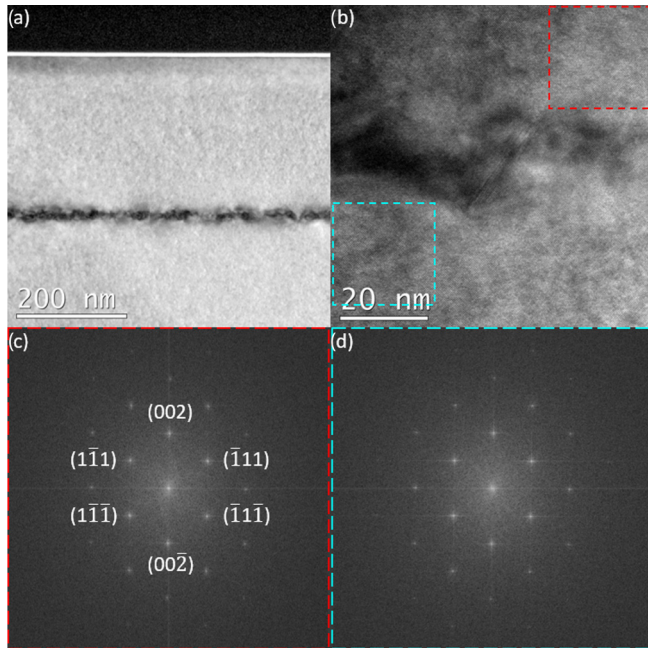
FIG. 6. Cross-sectional TEM images of a lamella of sample B after annealing. (a) The end of range defects are visible as a dark band ∼290 nm below the surface. (b) High-resolution TEM image showing the successful repair of the crystal lattice in the implanted layer. Crystal diffraction patterns of (c) the implanted region (highlighted in red) and (d) the nonimplanted region (highlighted in cyan).

Pt via electron-beam assisted deposition. This was followed by a 2.5 μm Pt layer deposited via a 30 keV Ga ion beam. A lamella was then extracted and thinned to a thickness of ∼100 nm, with a final polishing step performed with a 5 keV Ga ion beam that results in negligible implantation damage. A TEM (FEI, Tecnai TF20) was used to take high-resolution cross-sectional images in which a 200 keV electron beam was transmitted down the [110] direction through the lamella to view the atomic arrangement. The TEM images and diffraction patterns are shown in Fig. 6.

End of range defects, visible as a dark band ∼290 nm below the surface in Fig. 6(a), indicate the location of the a/c interface before annealing. The a-Si layer is extended to greater depths during continued ion bombardment above the Si amorphization threshold [66] (typically around 1×10^{15} cm^{-2} for keV Si ions [67]). The end of range defects are significantly deeper than the peak in the impurity concentration observed in Fig. 5(b). The open volume defects that getter impurities are invisible to TEM and occur in a region of vacancy excess at an intermediate depth between the surface and end of range [64]. The excess of interstitials at the end of range produced during ion implantation can evolve into dislocation loops during SPE regrowth of the a-Si layer [68]. These dislocation loops are stable up to temperatures of 1100 °C [69], whereby they release self-interstitials into the surrounding substrate. This could cause undesired transient-enhanced diffusion [70] of implanted P donor qubits in this enriched layer, and so lower thermal budgets, supplied by low-temperature SPE and rapid donor activation anneals, are preferred.

Fast Fourier transforms (FFTs) of regions of the TEM image in Fig. 6(b) were taken to give diffraction patterns indicating the crystal structure of the lamella. The diffraction pattern for the implanted region, shown in Fig. 6(c), indicates a crystal quality that matches that of the nonimplanted c-Si substrate beneath, shown in Fig. 6(d). This shows the success of the crystallization during postimplantation annealing. The contamination level introduced during the high fluence implantation is therefore low enough to avoid the formation of a polycrystalline ^{28}Si layer, which would contain undesirable charge traps and dangling bonds at grain boundaries [71]. We expect that this single-crystal layer of isotopically enriched ^{28}Si will provide an ideal environment for implanted donor qubits, with high activation and long coherence times. This awaits confirmation with a high sensitivity ESR measurement of a low concentration ($\leqslant 1 \times 10^{16}$ cm^{-3}) of donors implanted into this ^{28}Si surface layer. A single donor coherence time measurement with a single electron transistor [7] would provide the ultimate test for the ^{28}Si material.

VI. CONCLUSION

In conclusion, a Hahn echo measurement of P donors implanted into a ^{28}Si layer with ∼3000 ppm ^{29}Si, produced by high fluence implantation of 30 keV ^{28}Si^{-} ions, was fitted with a monoexponential decay, suggesting an isotopically enriched ^{28}Si donor environment. The extracted coherence time of $T_2 = 285 \pm 14$ μs is longer than that found with ^{nat}Si for similar P concentrations. The residual level of ^{29}Si was further decreased by implanting 45 keV ^{28}Si^{-} ions in the one-for-one sputtering regime. A high fluence (2.63×10^{18} cm^{-2}) implant of ^{28}Si^{-} ions at this energy into ^{nat}Si results in a depletion of ^{29}Si down to 250 ppm in a surface layer of thickness ∼100 nm, as measured with SIMS. The drastically reduced concentration of ^{29}Si spin-1/2 nuclei in this isotopically enriched layer should further extend the coherence time of implanted donors beyond that achieved with commercial Isonics ^{28}Si epilayers. Care was taken to limit the level of contamination introduced during high fluence implantation, and concentrations were found to be below 1×10^{17} cm^{-3} for C and 3×10^{17} cm^{-3} for O, comparable to those in Czochralski-grown Si. The levels of contamination in this isotopically enriched a-Si layer are low enough to allow for successful crystallization by SPE. The quality of the single-crystal surface layer of ^{28}Si was shown to be equivalent to the nonimplanted region of the c-Si substrate using high-resolution TEM, in which the end of range defects were still visible after annealing. This work shows that the high fluence implantation of ^{28}Si^{-} ions at energies around 45 keV is an effective method for isotopic enrichment, which could be incorporated *in situ* into the fabrication of ion implanted donor spins in ^{28}Si for quantum devices with increased coherence times.

[1] B. E. Kane, Nature (London) **393**, 133 (1998).

[2] D. Loss and D. P. DiVincenzo, Phys. Rev. A **57**, 120 (1998).

[3] F. A. Zwanenburg, A. S. Dzurak, A. Morello, M. Y. Simmons, L. C. L. Hollenberg, G. Klimeck, S. Rogge, S. N. Coppersmith, and M. A. Eriksson, Rev. Mod. Phys. **85**, 961 (2013).

[4] P. A. De Groot, *Handbook of Stable Isotope Analytical Techniques* (Elsevier, Amsterdam, 2004), Vol. 1.

[5] R. de Sousa and S. Das Sarma, Phys. Rev. B **68**, 115322 (2003).

[6] W. M. Witzel, M. S. Carroll, A. Morello, Ł. Cywiński, and S. Das Sarma, Phys. Rev. Lett. **105**, 187602 (2010).

[7] J. J. Pla, K. Y. Tan, J. P. Dehollain, W. H. Lim, J. J. L. Morton, D. N. Jamieson, A. S. Dzurak, and A. Morello, Nature (London) **489**, 541 (2012).

[8] J. J. Pla, K. Y. Tan, J. P. Dehollain, W. H. Lim, J. J. L. Morton, F. A. Zwanenburg, D. N. Jamieson, A. S. Dzurak, and A. Morello, Nature (London) **496**, 334 (2013).

[9] W. Kohn and J. M. Luttinger, Phys. Rev. **98**, 915 (1955).

[10] K. M. Itoh and H. Watanabe, MRS Commun. **4**, 143 (2014).

[11] J. T. Muhonen, J. P. Dehollain, A. Laucht, F. E. Hudson, R. Kalra, T. Sekiguchi, K. M. Itoh, D. N. Jamieson, J. C. McCallum, A. S. Dzurak *et al.*, Nat. Nanotechnol. **9**, 986 (2014).

[12] W. S. Capinski, H. J. Maris, E. Bauser, I. Silier, M. Asen-Palmer, T. Ruf, M. Cardona, and E. Gmelin, Appl. Phys. Lett. **71**, 2109 (1997).

[13] T. Ruf, R. W. Henn, M. Asen-Palmer, E. Gmelin, M. Cardona, H.-J. Pohl, G. G. Devyatych, and P. G. Sennikov, Solid State Commun. **115**, 243 (2000).

[14] A. V. Inyushkin, A. N. Taldenkov, J. W. Ager III, E. E. Haller, H. Riemann, N. V. Abrosimov, H.-J. Pohl, and P. Becker, J. Appl. Phys. **123**, 095112 (2018).

[15] I. C. Kizilyalli, H. Safar, J. Herbsommer, S. J. Burden, and P. L. Gammel, IEEE Electron Device Lett. **26**, 404 (2005).

[16] K.-i. Takyu, K. M. Itoh, K. Oka, N. Saito, and V. I. Ozhogin, Jpn. J. Appl. Phys. **38**, L1493 (1999).

[17] A. D. Bulanov, G. G. Devyatych, A. V. Gusev, P. G. Sennikov, H.-J. Pohl, H. Riemann, H. Schilling, and P. Becker, Cryst. Res. Technol.: J. Exp. Indust. Crystallogr. **35**, 1023 (2000).

[18] K. M. Itoh, J. Kato, M. Uemura, A. K. Kaliteevskii, O. N. Godisov, G. G. Devyatych, A. D. Bulanov, A. V. Gusev, I. D. Kovalev, P. G. Sennikov *et al.*, Jpn. J. Appl. Phys. **42**, 6248 (2003).

[19] P. Becker, H. Friedrich, K. Fujii, W. Giardini, G. Mana, A. Picard, H.-J. Pohl, H. Riemann, and S. Valkiers, Meas. Sci. Technol. **20**, 092002 (2009).

[20] P. Becker, H.-J. Pohl, H. Riemann, and N. V. Abrosimov, Physica Status Solidi A **207**, 49 (2010).

[21] P. G. Sennikov, A. V. Vodopyanov, S. V. Golubev, D. A. Mansfeld, M. N. Drozdov, Y. N. Drozdov, B. A. Andreev, L. V. Gavrilenko, D. A. Pryakhin, V. I. Shashkin *et al.*, Solid State Commun. **152**, 455 (2012).

[22] N. V. Abrosimov, D. G. Aref'ev, P. Becker, H. Bettin, A. D. Bulanov, M. F. Churbanov, S. V. Filimonov, V. A. Gavva, O. N. Godisov, A. V. Gusev *et al.*, Metrologia **54**, 599 (2017).

[23] V. Mazzocchi, P. G. Sennikov, A. D. Bulanov, M. F. Churbanov, B. Bertrand, L. Hutin, J. P. Barnes, M. N. Drozdov, J. M. Hartmann, and M. Sanquer, J. Cryst. Growth **509**, 1 (2019).

[24] D. Sabbagh, N. Thomas, J. Torres, R. Pillarisetty, P. Amin, H. C. George, K. Singh, A. Budrevich, M. Robinson, D. Merrill *et al.*, Phys. Rev. Appl. **12**, 014013 (2019).

[25] T. Kojima, R. Nebashi, K. M. Itoh, and Y. Shiraki, Appl. Phys. Lett. **83**, 2318 (2003).

[26] H. Bracht, N. Wehmeier, S. Eon, A. Plech, D. Issenmann, J. Lundsgaard Hansen, A. Nylandsted Larsen, J. W. Ager III, and E. E. Haller, Appl. Phys. Lett. **101**, 064103 (2012).

[27] Y. Nakabayashi, T. Segawa, H. I. Osman, K. Saito, S. Matsumoto, J. Murota, K. Wada, and T. Abe, Jpn. J. Appl. Phys. **39**, L1133 (2000).

[28] J. L. O'Brien, S. R. Schofield, M. Y. Simmons, R. G. Clark, A. S. Dzurak, N. J. Curson, B. E. Kane, N. S. McAlpine, M. E. Hawley, and G. W. Brown, Phys. Rev. B **64**, 161401(R) (2001).

[29] L. Oberbeck, N. J. Curson, M. Y. Simmons, R. Brenner, A. R. Hamilton, S. R. Schofield, and R. G. Clark, Appl. Phys. Lett. **81**, 3197 (2002).

[30] K. J. Dwyer, J. M. Pomeroy, D. S. Simons, K. L. Steffens, and J. W. Lau, J. Phys. D **47**, 345105 (2014).

[31] K. Tang, H. S. Kim, A. N. Ramanayaka, D. S. Simons, and J. M. Pomeroy, J. Phys. Commun. **4**, 035006 (2020).

[32] N. Tsubouchi, A. Chayahara, Y. Mokuno, A. Kinomura, and Y. Horino, Jpn. J. Appl. Phys. **40**, L1283 (2001).

[33] G. Tosi, F. A. Mohiyaddin, V. Schmitt, S. Tenberg, R. Rahman, G. Klimeck, and A. Morello, Nat. Commun. **8**, 450 (2017).

[34] J. Van Donkelaar, C. Yang, A. D. C. Alves, J. C. McCallum, C. Hougaard, B. C. Johnson, F. E. Hudson, A. S. Dzurak, A. Morello, D. Spemann *et al.*, J. Phys.: Condens. Matter **27**, 154204 (2015).

[35] R. J. Schreutelkamp, J. S. Custer, J. R. Liefting, W. X. Lu, and F. W. Saris, Mater. Sci. Rep. **6**, 275 (1991).

[36] D. Holmes, W. I. L. Lawrie, B. C. Johnson, A. Asadpoordarvish, J. C. McCallum, D. R. McCamey, and D. N. Jamieson, Phys. Rev. Mater. **3**, 083403 (2019).

[37] X. Zhu, J. S. Williams, and J. C. McCallum, Nucl. Instrum. Methods Phys. Res., Sect. B **148**, 268 (1999).

[38] X. Zhu, J. S. Williams, and J. C. McCallum, Appl. Phys. Lett. **73**, 1811 (1998).

[39] M. Radek, H. Bracht, B. C. Johnson, J. C. McCallum, M. Posselt, and B. Liedke, Appl. Phys. Lett. **107**, 082112 (2015).

[40] E. F. Kennedy, L. Csepregi, J. W. Mayer, and T. W. Sigmon, J. Appl. Phys. **48**, 4241 (1977).

[41] J. S. Williams, in *Surface Modification and Alloying* (Springer, Boston, MA, 1983), pp. 133–163.

[42] G. L. Olson and J. A. Roth, Mater. Sci. Rep. **3**, 1 (1988).

[43] G. E. Jellison, Jr. and F. A. Modine, J. Appl. Phys. **76**, 3758 (1994).

[44] J. Roth, G. Olson, D. Jacobson, and J. Poate, Appl. Phys. Lett. **57**, 1340 (1990).

[45] X. Zhu, J. S. Williams, D. J. Llewellyn, and J. C. McCallum, Appl. Phys. Lett. **74**, 2313 (1999).

[46] J. F. Ziegler, M. D. Ziegler, and J. P. Biersack, Nucl. Instrum. Methods Phys. Res., Sect. B **268**, 1818 (2010).

[47] T. Kobayashi, J. Salfi, C. Chua, J. van der Heijden, M. G. House, D. Culcer, W. D. Hutchison, B. C. Johnson, J. C. McCallum, H. Riemann *et al.*, Nat. Mater. **20**, 38 (2021).

[48] S. Weichselbaumer, P. Natzkin, C. W. Zollitsch, M. Weiler, R. Gross, and H. Huebl, Phys. Rev. Appl. **12**, 024021 (2019).

[49] G. Feher, Phys. Rev. **114**, 1219 (1959).

[50] A. M. Tyryshkin, S. Tojo, J. J. L. Morton, H. Riemann, N. V. Abrosimov, P. Becker, H.-J. Pohl, T. Schenkel, M. L. W. Thewalt, K. M. Itoh *et al.*, Nat. Mater. **11**, 143 (2012).

[51] A. M. Tyryshkin, S. A. Lyon, A. V. Astashkin, and A. M. Raitsimring, Phys. Rev. B **68**, 193207 (2003).

[52] M. Chiba and A. Hirai, J. Phys. Soc. Jpn. **33**, 730 (1972).

[53] E. Abe, A. M. Tyryshkin, S. Tojo, J. J. L. Morton, W. M. Witzel, A. Fujimoto, J. W. Ager, E. E. Haller, J. Isoya, S. A. Lyon, M. L. W. Thewalt, and K. M. Itoh, Phys. Rev. B **82**, 121201(R) (2010).

[54] J. P. Gordon and K. D. Bowers, Phys. Rev. Lett. **1**, 368 (1958).

[55] W. Möller, W. Eckstein, and J. P. Biersack, Comput. Phys. Commun. **51**, 355 (1988).

[56] W. Möller and W. Eckstein, Nucl. Instrum. Methods Phys. Res., Sect. B **7**, 645 (1985).

[57] H. H. Andersen and H. L. Bay, J. Appl. Phys. **46**, 1919 (1975).

[58] O. Fröhlich, H. Baumann, and K. Bethge, Nucl. Instrum. Methods Phys. Res., Sect. B **50**, 436 (1990).

[59] W. Eckstein, in *Sputtering by Particle Bombardment* (Springer, Berlin, Heidelberg, 2007), pp. 33–187.

[60] S. G. Robson, A. M. Jakob, D. Holmes, S. Q. Lim, B. C. Johnson, and D. N. Jamieson, Nucl. Instrum. Methods Phys. Res., Sect. B **487**, 1 (2021).

[61] I. L. Singer and T. M. Barlak, Appl. Phys. Lett. **43**, 457 (1983).

[62] H. M. Liaw, Microelectron. J. **12**, 33 (1981).

[63] M. Tamura, T. Ando, and K. Ohyu, Nucl. Instrum. Methods Phys. Res., Sect. B **59**, 572 (1991).

[64] R. A. Brown, O. Kononchuk, G. A. Rozgonyi, S. Koveshnikov, A. P. Knights, P. J. Simpson, and F. Gonzalez, J. Appl. Phys. **84**, 2459 (1998).

[65] M. Servidori, R. Angelucci, F. Cembali, P. Negrini, S. Solmi, P. Zaumseil, and U. Winter, J. Appl. Phys. **61**, 1834 (1987).

[66] A. Claverie, C. Vieu, J. Faure, and J. Beauvillain, J. Appl. Phys. **64**, 4415 (1988).

[67] H. Mori, S. Adachi, and M. Takahashi, J. Appl. Phys. **90**, 87 (2001).

[68] K. S. Jones, S. Prussin, and E. R. Weber, Appl. Phys. A **45**, 1 (1988).

[69] G. Z. Pan, K.-N. Tu, and S. Prussin, Appl. Phys. Lett. **71**, 659 (1997).

[70] P. A. Stolk, H.-J. Gossmann, D. J. Eaglesham, D. C. Jacobson, C. S. Rafferty, G. H. Gilmer, M. Jaraiz, J. M. Poate, H. S. Luftman, and T. E. Haynes, J. Appl. Phys. **81**, 6031 (1997).

[71] C. H. Seager, Annu. Rev. Mater. Sci. **15**, 271 (1985).